International Journal of Heat and Mass Transfer 52 (2009) 996–1004

Contents lists available at ScienceDirect

International Journal of Heat and Mass Transfer

journal homepage: www.elsevier.com/locate/ijhmt

Unsteady heat conduction involving phase changes for an irregular bubble/particle entrapped in a solid during freezing – An extension of the heat-balance integral method

K.R. Lin, P.S. Wei *, S.Y. Hsiao

Department of Mechanical and Electro-Mechanical Engineering, National Sun Yat-Sen University, Kaohsiung 80424, Taiwan, ROC

ARTICLE INFO

Article history:
Received 13 June 2007
Received in revised form 2 July 2008
Available online 21 September 2008

Keywords:
Integral method
Heat-balance integral method
Pore formation
Porosity
Bubble capture
Particle inclusion
Contact melting

ABSTRACT

Temperature distributions in the molten layer and solid with distinct properties around a bubble or particle entrapped in the solid during unidirectional solidification are determined by applying a heat-balance integral approximation method. The present model can be used to simulate growth, entrapment or departure of a bubble or particle inclusion in solids encountered in manufacturing and materials processing, MEMS, contact melting processes, drilling, etc. In this work, the proposed heat-balance equations are derived by integrating unsteady elliptic heat diffusion equations and introducing the Stefan boundary condition. Due to the time-dependent irregular shapes of phases, coefficients of assumed quadratic temperature profiles are considered to be functions of longitudinal coordinate and time. Temperature coefficients in distinct regions therefore are determined by solving equations governing temperature coefficients derived from heat-balance equations, imposing boundary conditions, and introducing a fictitious boundary condition. The computed temperature fields show agreement with predictions from the finite-difference method. Since the number of independent variables is reduced by one, this work provides an effective method to solve unsteady elliptic diffusion problems experiencing solid–liquid phase changes in irregular shapes.

1. Introduction

The heat conduction or diffusion problems involving phase transition between solid and liquid (called the Stefan problem) are nonlinear, because the moving boundaries must be determined along with the solution. Except for several cases [1,2], these problems are not amenable to analytical solutions. Approximate integral methods therefore are much easier to manipulate, as extensively reviewed by Goodman [3] and Crank [2], because the number of independent variables is reduced by one after an integration. Approximate integral methods, for example, the Karman–Pohlhausen method, have been widely and effectively used in the field of boundary layer theory in fluid dynamics [4]. The nonlinear, parabolic transport differential equations after integration across the spatial variable transverse to the stream direction and introduction an assumed velocity profile will thereby reduce to a first-order ordinary differential equation for the boundary layer thickness. Using a marching technique, boundary layer thickness as well as velocity profiles can be readily obtained.

Goodman [5] applied a similar integral method to study different transient one-phase, single spatial dimension ice-melting problems. He assumed a second-degree polynomial in the spatial variable for temperature profile, comprising unknown time-dependent coefficients analytically determined by satisfying boundary conditions. A heat-balance equation was then obtained by integrating the heat conduction equation over the thermal boundary layer and introducing the assumed temperature profile and Stefan boundary condition at the solid–liquid interface. The heat-balance equation can be integrated to find the phase-change boundary, leading to the time-dependent temperature distribution. This method provides accurate, general and easy solutions.

Goodman and Shea [6] further applied the heat-balance method to the two-phase problem of melting a finite slab that is initially at a uniform temperature below the melting point. Heat conduction equations of the liquid and solid were, respectively, integrated over their own phases. Summing the heat-balance equations of the liquid and solid and introducing the Stefan boundary condition gave the total heat-balance equation. The time-dependent coefficients of the assumed quadratic temperature profiles in the liquid and solid were analytically determined from the boundary conditions and the heat-balance equation of its own phase. Three coupled ordinary differential equations including the total

* Corresponding author. Tel.: +886 7 5254050/5321272; fax: +886 7 5254214/5254299.
E-mail address: pswei@mail.nsysu.edu.tw (P.S. Wei).

0017-9310/$ - see front matter © 2008 Elsevier Ltd. All rights reserved.
doi:10.1016/j.ijheatmasstransfer.2008.07.034

Nomenclature

a, b, c, a', b'	temperature coefficients
f	fictitious thickness beyond solidification front, as illustrated in Fig. 2
g	temperature gradient, $g^* \equiv gr_0/(T_i - T_m)$, defined in Eq. (11)
$\bar{h}$	mean heat transfer coefficient
H	energy function, $H^* = H/[(T_i - T_m)r_0^3]$, defined in Eq. (14)
K	k_l/k_s
L	latent heat
Nu	Nusselt number $\equiv \bar{h}r_0/k_l$
r	spherical radial coordinate, $r^* \equiv r/r_0$, as illustrated in Fig. 1
R	outside radius of system, $R^* \equiv R/r_0$, as illustrated in Fig. 1
r_0	initial radius of curvature at axisymmetric axis
s	location of solidification front, $s^* \equiv s/r_0$, as illustrated in Fig. 1
Ste	Stefan number $\equiv c_p(T_i - T_m)/L$
t^*	dimensionless time $\equiv t\alpha_l/r_0^2$
U	solidification speed = ds/dt
x, z	coordinates in horizontal and upward directions, as illustrated in Fig. 1

Greek letters

Γ	α_l/α_s
δ	molten layer thickness $\equiv r_m - r_i$, $\delta^* \equiv \delta/r_0$
θ	polar angle in spherical coordinates, as illustrated in Fig. 1
ψ	dimensionless temperature $\equiv (T - T_m)/(T_i - T_m)$

Subscripts

c	cold bottom
e	edge
f	fictitious region
i	inner surface, namely, bubble or particle surface
l	liquid
m	melting
R	outer boundary
s	solid
0	initial time

Superscript

*	dimensionless quantity

heat-balance equation and integrated temperatures for two phases were solved by using a power series method.

Most previous investigations were confined to transient one-dimensional problems. Poots [7] therefore extended the heat-balance integral method to solve a two-dimensional, one-phase problem related to solidification of a liquid, initially at the fusion temperature, contained in a uniform prism of square cross-section. The surface was suddenly maintained at a constant temperature below the fusion temperature. The heat-balance equations involved complicated surface and volume integrations. The three-dimensional freezing of a cuboid was similarly extended by Riley and Duck [8]. The expressions for the two- or three-dimensional profiles and the resulted heat-balance equations, however, were cumbersome.

Rasmussen [9] extended the heat-balance integral method to solve a transient, two-dimensional, one-phase heat conduction problem. Instead of a single two-dimensional global profile, the temperature field in the solid was chosen to be a set of one-dimensional profiles at pre-selected locations on the direction transverse to the freezing direction. The coefficient of the temperature profile was reciprocal of interface location, which was a function of time and transverse coordinate. The linear profiles, however, are hardly suited to practical problems. The heat-balance equation was then obtained by integrating over the liquid phase along the freezing direction. Kharab [10] extended the unsteady two-dimensional model provided by Rasmussen [9] and introduced a quadratic temperature profile to predict a transient three-dimensional temperature field in a cuboid. To determine the coefficients and interface location as functions of two spatial variables and time, the zeroth and first momentum of the heat conduction equation were used. This led to complicated equations for the interfacial location that needed to be solved numerically.

The motivation of this work arisen from prediction of temperature fields in the solid and liquid surrounding a bubble growing after nucleation on the solidification front [11]. In view of the physical domains in irregular shapes, the most frequently used techniques to obtain a rectangular computational domain are immobilization transformation and grid generation methods. These, however, lead to many additional terms in solving unsteady heat conduction equations with two spatial coordinates and time [12,13]. The proposed integral method in this work can be efficiently used to simulate nucleation and growth of a bubble on a solidification front [11,14–24], departure or capture of a particle on a solidification front [25–29], contact melting [30–33], drilling processes [34–36], etc.

In this work, temperature distributions around a bubble or particle surrounded by a molten layer in a solid produced in the course of unidirectional solidification are determined by applying the heat-balance integral method. Owing to transient irregular shapes of phases, the time- and angle-dependent coefficients of assumed temperature profiles are determined by solving total and heat-balance equations governing temperature coefficients, imposing real and fictitious boundary conditions in distinct regions. This present work provides a general and modified approximation method to solve unsteady elliptic diffusion equations in irregular domains experiencing phase changes.

2. System model and analysis

In this work, an axisymmetric tiny bubble (or particle) around 10^{-3}–10^{-6} m is emanated on the solidification front and entrapped in solid, as illustrated in Fig. 1. A spherical coordinate system is chosen with the origin at the same level as the solid–liquid interface at a time specified by $t = 0$. In view of the cold temperature T_c at the bottom location $z = z_c$, which is a negative value, the solid–liquid interface proceeds at a speed U in the positive z-direction. The bubble surface at $r = r_i$ maintains constant temperature T_i, while the temperature at $r = R$ far from the bubble is linear in z-direction. In this case, temperatures $T_c \leqslant T_m \leqslant T_i$ are considered. Heat thus can also be transferred from the liquid beyond the solidification front through the bubble into the solid, resulting in the formation of a thin liquid layer in a time-dependent thickness δ. At location $z = s$, there exist two different boundary conditions, which are the melting temperature at the solidification front ($r \geqslant r_m$) and the heat convection across the liquid layer ($r_i \leqslant r \leqslant r_m$).

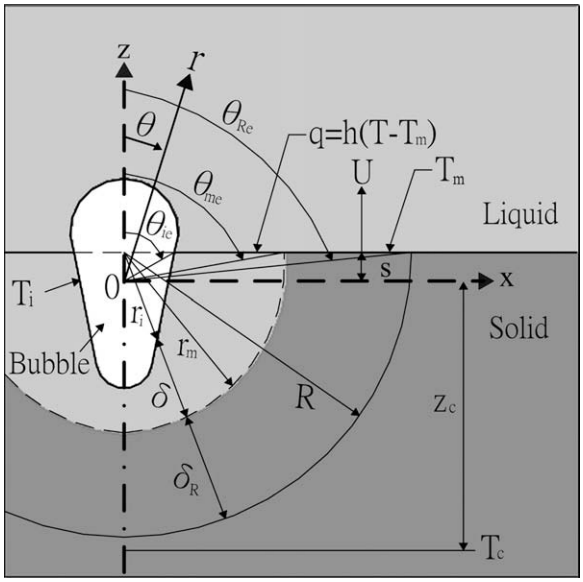

Fig. 1. System model physical domain and coordinate system.

2.1. Governing equations and boundary conditions

Without loss of generality, the major assumptions made are as follows:

1. This model is unsteady and axisymmetric.
2. Temperature at the bubble surface is uniform. This is because the Biot number, defined as the product of heat transfer coefficient and average or hydraulic bubble radius divided by thermal conductivity of the gas in the bubble, is approximately 0.001–0.01 [37,38].
3. The surface of the bubble (or particle) in the solid is independent of time to a first approximation, as confirmed by experimental observations [11,24]. In fact, the growth (or decay) of the bubble is due to a decrease (or increase) in time-dependent gas pressure in the bubble, resulted from mass transfer of solute gases accumulated around the bubble and ahead of the solidification front. However, the growth of the bubble surface is faster than the time scale of solidification. The effects of the time-dependent bubble surface on thermal fields thus are not so important. The frequently observed long columnar pores in a solid also reveal the nearly stationary bubble shape [18]. The present method is still applicable, provided that the bubble shape is time-dependent. Governing equations, however, become complicated, as discussed later.
4. Convection in the molten layer is neglected. Except for the perturbed body force due to gravity [39], the driving forces such as Marangoni and buoyancy forces responsible for convection are neglected due to a rather uniform surface temperature and small size of the microscale-sized and lumped bubble.
5. The solidification rate in the upward freezing is specified from experimental data [24]. Otherwise, a self-consistent solidification rate is determined by simultaneously solving energy equations for solid and liquid phases satisfied by Stefan boundary condition.
6. Temperature in the solid far from the bubble at any instantaneous time is a linear function of coordinate in the freezing direction.
7. Temperature profiles in the solid and the liquid are assumed to be quadratic in radial directions, while their coefficients are functions of longitudinal direction and time.
8. Thermal properties between the solid and liquid are allowed to be distinct and constant averaged within a reasonable temperature range considered.

With the above assumptions, unsteady, axisymmetric heat conduction equations in the liquid and solid, respectively, become

$$\frac{\partial T_l}{\partial t} = \alpha_l \nabla^2 T_l \tag{1}$$

$$\frac{\partial T_s}{\partial t} = \alpha_s \nabla^2 T_s \tag{2}$$

where the Laplacian operator is

$$\nabla^2 \equiv \frac{1}{r^2}\frac{\partial}{\partial r}\left(r^2\frac{\partial}{\partial r}\right) + \frac{1}{r^2\sin\theta}\frac{\partial}{\partial\theta}\left(\sin\theta\frac{\partial}{\partial\theta}\right) \tag{3}$$

Temperature at the bubble or inner surface is

$$T_l = T_i = \text{const. at } r = r_i(\theta) \quad \text{and} \quad \theta_{ie} \leqslant \theta \leqslant \pi \tag{4}$$

Temperature and balance of heat fluxes at the outer boundary of the liquid layer are, respectively, [38,40,41]

$$T_l = T_m = T_s, \quad -k_l\frac{\partial T_l}{\partial n} = \rho L v_n - k_s\frac{\partial T_s}{\partial n} \quad \text{at } r = r_m(\theta,t) \quad \text{and} \quad \theta_{me} \leqslant \theta \leqslant \pi \tag{5}$$

where the second equation is Stefan boundary condition indicating that heat conduction from liquid to the solid–liquid interface is balanced by latent heat for melting or freezing and heat conduction from the interface into solid. Velocity and normal gradient directed from liquid to solid at the interface in Eq. (5), respectively, are [38,40,41]

$$v_n = -\frac{\partial F}{\partial t}\Big/\|\nabla F\| = \frac{\partial r_m}{\partial t}\left[1+\left(\frac{1}{r_m}\frac{\partial r_m}{\partial\theta}\right)^2\right]^{-1/2} \tag{6}$$

$$\frac{\partial}{\partial n} = \mathbf{n}\cdot\nabla = \left[1+\left(\frac{1}{r_m}\frac{\partial r_m}{\partial\theta}\right)^2\right]^{-1/2}\left(\frac{\partial}{\partial r} - \frac{1}{r_m^2}\frac{\partial r_m}{\partial\theta}\frac{\partial}{\partial\theta}\right) \tag{7}$$

where the scalar function $F(r,\theta,t) = r - r_m(\theta,t) = 0$ delineates the contour of the liquid layer. Solidification takes place due to the cold temperature at the bottom, given by

$$T_s = T_c \quad \text{at } z = z_c \tag{8}$$

As mentioned previously, two boundary conditions are prescribed at the top boundary. They are, respectively, specification of heat convection across the liquid layer

$$-k_l\frac{\partial T_l}{\partial\theta} = \bar{h}r_0(T_l - T_m) \quad \text{for} \quad \theta_{ie} \leqslant \theta \leqslant \theta_{me} \text{ at } z = s(t) \tag{9}$$

which indicates that the downward heat transfer to the liquid layer is decreased across $z = s$ in the outward direction. The melting temperature at the solidification front

$$T_s = T_m \quad \text{for} \quad \theta_{me} \leqslant \theta \leqslant \theta_{Re} \text{ at } z = s(t) \tag{10}$$

A linear temperature profile in solid in the vertical direction far from the bubble is given by

$$T_s = T_m + g(t)(z - s(t)), \quad \text{where } g(t) \equiv \frac{T_m - T_c}{s(t) - z_c} \quad \text{at } R \leqslant r, \ z_c \leqslant z \leqslant s \tag{11}$$

which is satisfied by melting and cold temperatures at the solidification front ($z = s$) and bottom ($z = z_c$), and dependence of time, respectively.

2.2. Integral equations

Heat conduction equations (1) and (2) integrated along the radial direction, respectively, give

$$\frac{\partial H_l^*}{\partial t^*} = r_m^{*2}\frac{\partial \psi_l}{\partial r^*}\bigg|_{r_m^*} - r_i^{*2}\frac{\partial \psi_l}{\partial r^*}\bigg|_{r_i^*} + \frac{1}{\sin\theta}\int_{r_i^*}^{r_m^*}\frac{\partial}{\partial\theta}\left(\sin\theta\frac{\partial \psi_l}{\partial\theta}\right)dr^* \tag{12}$$

$$\Gamma\frac{\partial H_s^*}{\partial t^*} = R^{*2}\frac{\partial \psi_s}{\partial r^*}\bigg|_{R^*} - r_m^{*2}\frac{\partial \psi_s}{\partial r^*}\bigg|_{r_m^*} + \frac{1}{\sin\theta}\int_{r_m^*}^{R^*}\frac{\partial}{\partial\theta}\left(\sin\theta\frac{\partial \psi_s}{\partial\theta}\right)dr^* \tag{13}$$

where dimensionless energy functions of the liquid and solid are, respectively, defined as

$$H_l^* \equiv \int_{r_i^*(\theta)}^{r_m^*(\theta,t^*)}\psi_l r^{*2}\,dr^*, \quad H_s^* \equiv \int_{r_m^*(\theta,t^*)}^{R^*}\psi_s r^{*2}\,dr^* \tag{14}$$

Multiplying Eq. (12) by the conductivity ratio K, summing to Eq. (13), and introducing the Stefan boundary condition from Eq. (5) lead to the total energy equation

$$\begin{aligned} K\frac{\partial H_l^*}{\partial t^*} + \Gamma\frac{\partial H_s^*}{\partial t^*} = {} & \frac{\Gamma}{Ste}r_m^{*2}\frac{\partial r_m^*}{\partial t^*} + R^{*2}\frac{\partial \psi_s}{\partial r^*}\bigg|_{R^*} - Kr_i^{*2}\frac{\partial \psi_l}{\partial\partial r^*}\bigg|_{r_i^*} \\ & + \frac{1}{\sin\theta}\left[K\int_{r_i^*}^{r_m^*}\frac{\partial}{\partial\theta}\left(\sin\theta\frac{\partial \psi_l}{\partial\theta}\right)dr^* \right. \\ & \left. + \int_{r_m^*}^{R^*}\frac{\partial}{\partial\theta}\left(\sin\theta\frac{\partial \psi_s}{\partial\theta}\right)dr^*\right] \end{aligned} \tag{15}$$

Temperatures in the liquid and solid are assumed to be [3,5]

$$\psi_l = a_l(\theta,t^*)\left[r^* - r_m^*(\theta,t^*)\right] + b_l(\theta,t^*)\left[r^* - r_m^*(\theta,t^*)\right]^2 \tag{16}$$

$$\psi_s = a_s(\theta,t^*)\left[r^* - r_m^*(\theta,t^*)\right] + b_s(\theta,t^*)\left[r^* - r_m^*(\theta,t^*)\right]^2 \tag{17}$$

where the boundary of the liquid layer (see Fig. 1)

$$r_m^*(\theta,t^*) = r_i^*(\theta) + \delta^*(\theta,t^*) \tag{18}$$

Eqs. (16) and (17) are automatically satisfied by the melting temperature at the outer boundary of the liquid layer. Furthermore, the effects of boundary conditions in the longitudinal direction on temperature fields are accounted for by the coefficients as functions of the longitudinal coordinate θ. Substituting Eqs. (16), (17) and (14) into Eqs. (12) and (13), respectively, leads to

$$\begin{aligned} & \frac{\delta^{*3}}{3}\frac{\partial^2 b_l}{\partial\theta^2} + \left(\frac{\delta^*\cot\theta}{3} + 2\frac{\partial r_m^*}{\partial\theta}\right)\delta^{*2}\frac{\partial b_l}{\partial\theta} + 2\delta^*\left[\frac{\delta^* h_1}{2} + \left(\frac{\partial r_m^*}{\partial\theta}\right)^2 + r_i^{*2}\right]b_l \\ & - \frac{\delta^{*2}}{2}\frac{\partial^2 a_l}{\partial\theta^2} - \left(\frac{\delta^*\cot\theta}{2} + 2\frac{\partial r_m^*}{\partial\theta}\right)\delta^*\frac{\partial a_l}{\partial\theta} - \left(\delta^* h_1 - r_m^{*2} + r_i^{*2}\right)a_l = \frac{\partial H_l^*}{\partial t^*} \end{aligned} \tag{19}$$

$$\begin{aligned} & \frac{\delta_R^{*3}}{3}\frac{\partial^2 b_s}{\partial\theta^2} + \left(\frac{\delta_R^*\cot\theta}{3} - 2\frac{\partial r_m^*}{\partial\theta}\right)\delta_R^{*2}\frac{\partial b_s}{\partial\theta} + 2\delta_R^*\left[-\frac{\delta_R^* h_1}{2} + \left(\frac{\partial r_m^*}{\partial\theta}\right)^2 + R^{*2}\right]b_s \\ & + \frac{\delta_R^{*2}}{2}\frac{\partial^2 a_s}{\partial\theta^2} + \left(\frac{\delta_R^*\cot\theta}{2} - 2\frac{\partial r_m^*}{\partial\theta}\right)\delta_R^*\frac{\partial a_s}{\partial\theta} - \left(\delta_R^* h_1 + r_m^{*2} - R^{*2}\right)a_s = \Gamma\frac{\partial H_s^*}{\partial t^*} \end{aligned} \tag{20}$$

where the dimensionless quantities and energy functions of liquid and solid are, respectively,

$$\delta_R^* \equiv R^* - r_m^* \tag{21}$$

$$h_1 \equiv \frac{\partial^2 r_m^*}{\partial\theta^2} + \frac{\partial r_m^*}{\partial\theta}\cot\theta \tag{22}$$

$$H_l^* = a_l\left(\frac{r_m^* r_i^{*3}}{3} - \frac{r_i^{*4}}{4} - \frac{r_m^{*4}}{12}\right) + b_l\left(\frac{r_m^{*5}}{30} - \frac{r_m^{*2}r_i^{*3}}{3} + \frac{r_i^{*4}r_m^*}{2} - \frac{r_i^{*5}}{5}\right) \tag{23}$$

$$H_s^* = a_s\left(\frac{R^{*4}}{4} - \frac{r_m^* R^{*3}}{3} + \frac{r_m^{*4}}{12}\right) + b_s\left(\frac{R^{*5}}{5} - \frac{R^{*4}r_m}{2} + \frac{R^{*3}r_m^{*2}}{3} - \frac{r_m^{*5}}{30}\right) \tag{24}$$

The total energy from Eq. (15) by introducing Eqs. (19)–(24) is simplified to

$$\frac{\Gamma}{Ste}\frac{\partial r_m^*}{\partial t^*} = \left[\frac{1}{r_m^{*2}}\left(\frac{\partial r_m^*}{\partial\theta}\right)^2 + 1\right](a_s - Ka_l) \tag{25}$$

which is actually the Stefan boundary condition. This is because terms a_s and a_l on the right-hand side, respectively, represent solid and liquid temperature gradients at the solid–liquid interface, as can be seen from the leading terms of Eqs. (16) and (17).

2.3. Determination of temperature coefficients in liquid layer

In order to solve Eq. (19), boundary conditions are required. A relation between coefficients of temperature in the liquid layer is found to be

$$a_l = b_l\delta^* - \frac{1}{\delta^*} \tag{26}$$

which is obtained by substituting boundary condition equation (4) into Eq. (16). Boundary condition equation (9) by introducing Eq. (16) leads to

$$\begin{aligned} & \frac{\partial a_l}{\partial\theta} - \frac{a_l}{r^* - r_m^*}\frac{\partial r_m^*}{\partial\theta} + \frac{\partial b_l}{\partial\theta}(r^* - r_m^*) - 2b_l\frac{\partial r_m^*}{\partial\theta} \\ & = -Nu\left[a_l + b_l(r^* - r_m^*) - \frac{\psi_c}{r^* - r_m^*}\right] \end{aligned} \tag{27}$$

The axisymmetric boundary condition $\partial b_l/\partial\theta = 0$ at $\theta = \pi$ is also needed.

2.4. Determination of temperature coefficients in solid

The relation between temperature coefficients at the solidification front for angle $\theta_{me} \leqslant \theta \leqslant \theta_{Re}$ used for solving Eq. (20) is

$$a_s = -b_s\left(\frac{s^*}{\cos\theta} - r_m^*\right) \tag{28}$$

which is obtained by substituting Eq. (10) into Eq. (17). Since the assumed temperature profile is automatically satisfied at the outer boundary of the liquid layer, the other relation is needed to uniquely determine temperature coefficients of solid. In this work, it is proposed by introducing a fictitiously solid layer beyond the solidification front, as illustrated in Fig. 2, with the temperature profile from Eq. (17). This leads to

$$\psi_f = a_s\left(\frac{s^* + f}{\cos\theta} - r_m^*\right) + b_s\left(\frac{s^* + f}{\cos\theta} - r_m^*\right)^2 \tag{29}$$

The effects of the fictitious boundary condition equation (29) on temperature fields are presented later. Substituting the linear temperature profile as proposed by Eq. (11) into Eq. (17) leads to

$$a_s = g^*\frac{R^*\cos\theta - s^*}{R^* - r_m^*} - b_s(R^* - r_m^*) \tag{30}$$

The axisymmetric condition $\partial b_s/\partial\theta = 0$ at $\theta = \pi$.

Initial temperature coefficients a_{l0}, b_{l0}, a_{s0}, b_{s0} are determined from specification of initial temperature distributions in the liquid layer and solid. Derivations are presented in Appendix A.

2.5. Numerical method

Eq. (19) (and Eq. (20)) can be cast into

$$A_1\frac{\partial^2 b_l}{\partial\theta^2} + A_2\frac{\partial b_l}{\partial\theta} + A_3 b_l + A_4\frac{\partial^2 a_l}{\partial\theta^2} + A_5\frac{\partial a_l}{\partial\theta} + A_6 a_l = \frac{\partial H_l^*}{\partial t^*} \tag{31}$$

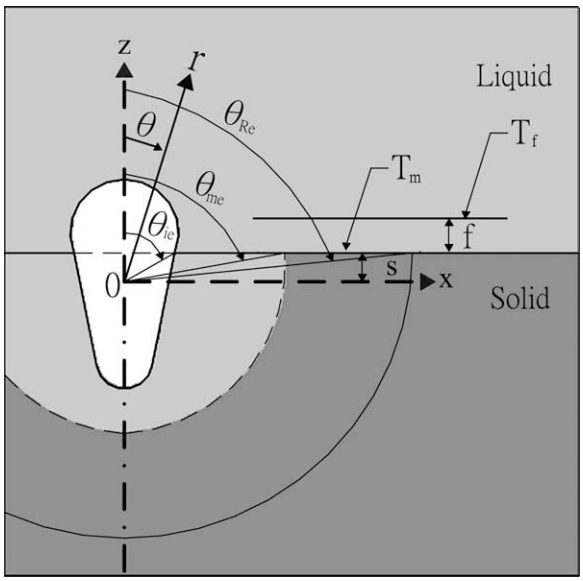

Fig. 2. Determination of temperature coefficients a_s and b_s for $\theta_{me} \leqslant \theta \leqslant \theta_{Re}$.

where the second and fifth terms on the left-hand side can be considered as convection terms, so that an upwind difference is used for discretization [42,43]. That is, the backward difference is used for a positive coefficient. Otherwise, the forward difference is adopted for a negative coefficient. The procedure to calculate thickness of the liquid layer and temperature fields around the bubble is described as follows:

1. Working parameters Stefan number, thermal conductivity and diffusivity ratios, cooling and melting temperatures, initial temperature fields, and $r_i^*(\theta), R^*, z_c^*, g_0^*, f, b, b'$, etc. are specified.
2. $H_{l0}^*, H_{s0}^*, a_{l0}, b_{l0}, a_{s0}$ and b_{s0} are, respectively, calculated from Eqs. (A4), (A10), (A6), (A5), (A12) and (A11).
3. Eqs. (25), (18) and (21) are, respectively, used to calculate r_m^*, δ^* and δ_R^*.
4. Coefficient b_l in Eq. (19) is numerically integrated over angles $\theta_{me} \leqslant \theta \leqslant \pi$ subject to Eq. (26), the axisymmetric condition, and Eq. (27) at θ_{me}. Coefficients in the range $\theta_{ie} \leqslant \theta \leqslant \theta_{me}$ are calculated from Eqs. (26) and (27).
5. Coefficient b_s in Eq. (20) is numerically integrated over angles $\theta_{Re} \leqslant \theta \leqslant \pi$ subject to Eq. (30), the axisymmetric condition, and Eq. (28) at θ_{Re}. Coefficients in the range $\theta_{me} \leqslant \theta \leqslant \theta_{Re}$ are calculated from Eqs. (28) and (29).
6. Steps 3–5 are repeated until convergence is achieved.
7. Temperature and energy fields in the liquid layer and solid are calculated from Eqs. (16), (17), (23) and (24), respectively.
8. Go to the next time and perform Steps 3–7.

3. Results and discussion

In this work, the independent dimensionless parameters governing temperature fields around a bubble or particle surrounded by a molten layer and entrapped in a solid produced during unidirectional solidification are the following: thermal conductivity and diffusivity ratios between liquid and solid (K and Γ), Stefan number (Ste), Nusselt number (Nu), and parameters governing bubble or particle shape, solidification rate, solid temperature gradient and cold temperature. Based on an initial radius of curvature at the axisymmetric axis $r_0 = 5 \times 10^{-4}$ m, solidification rate $U = 10^{-5}$ m/s, dimensionless independent parameters estimated are $K = 0.5$, $\Gamma = 0.5$, $Ste = 0.0167$, $Nu = 4.55 \times 10^{-4}$, $R^* = 40$, $z_c^* = -100$, $f = 62$, $\psi_c = -10$. Dimensionless temperature at location $z^* = s^* + f$ is $\psi_f = g_f^* f$ in a fictitious solid layer beyond the solidification front. In fact, this condition implies specified heat flux at the solidification front. The temperature gradient in the fictitious solid layer, for simplicity, is assumed to be identical to that in the bulk solid, $g_f^* = g^*$. The contour of the inner surface (namely, bubble or particle surface) $r^* = r_i^*$ is assumed to be a paraboloid of revolution given by

$$r_i^* = 1 + c(\pi - \theta)^2 \tag{32}$$

where coefficient $c = 0.2$. Provided that the bubble surface is time dependent, Eq. (32) can be replaced by the Rayleigh–Plesset or the Young–Laplace equation [44]. The time-dependent bubble shape therefore is affected by gas pressure in the bubble, as well as liquid and capillary pressures. The computation, however, becomes quite difficult.

Initial conditions for the integral method are specified in accordance with the finite-difference solutions of enthalpy equations provided by Lin [45]. Given temperatures of the bubble and solid, the higher temperature of the bubble heats the solid until a liquid layer occurs. Curve-fitting the contour of the liquid layer around the bubble at a chosen time gives the initial condition for the boundary between solid and liquid. That is

$$r_{m0}^* = 16.8433 - 20.4789\theta + 11.1423\theta^2 - 2.81269\theta^3 + 0.272755\theta^4 \tag{33}$$

The corresponding initial dimensionless temperature distributions in the liquid and solid are specified from Eqs. (A3) and (A9), respectively, by choosing $b = -2.4$ and $b' = -10^{-5}$ to simulate finite-difference solutions of enthalpy equations.

A successive over-relaxation method with a relaxation factor of 1.1 was used to solve an implicit finite-difference form of Eq. (31) governing time- and angle-dependent temperature coefficients [42,43]. Temperature fields thus are determined after coefficients are found at each time. Computations required convergence of temperature fields to be less than a relative error of 10^{-4}. The effects of different grid systems ($N_\theta \times N_r \times \Delta t^*$) with uniform spaces in longitudinal and radial directions and time on temperature fields are shown in Fig. 3(a)–(c), respectively. It can be seen that using time step $\Delta t^* = 4$ leads to very different temperature profiles, particularly near the solidification front and middle region of the solid phase. Relative deviation was found to be less than 1% by changing nodal points from 21 to 41 in the longitudinal direction, and the dimensionless time step from 0.4 to 0.04, respectively. The effect of nodal points from 21 to 41 in the radial direction is slight. Hence, thermal fields computed by choosing $N_\theta = 21$, $N_r = 41$, and $\Delta t^* = 0.4$ are sufficiently accurate for prediction in this work, as can also be seen in Fig. 3(d).

A comparison of predicted dimensionless temperature fields and liquid layer shapes between finite-difference method [45] and this work is presented in Fig. 4. The finite-difference method was used to solve enthalpy formulation of the energy equation. In contrast to often-used immobilization transformations for the governing equations in distinct phases satisfied by Stefan boundary condition, which lead to many additional terms, the enthalpy formation valid for different phases in the original coordinate system is efficient for dealing with phase transition between solid and liquid. The enthalpy method, however, still exhibits difficulties owing to the irregular physical domains. This work therefore extends the simpler heat-balance integral approximation method to solve elliptic equations in time-dependent irregular domains experiencing phase transitions in different regions. The major advantage of this method is that the number of independent variables is reduced by one after applying integration. In this figure,

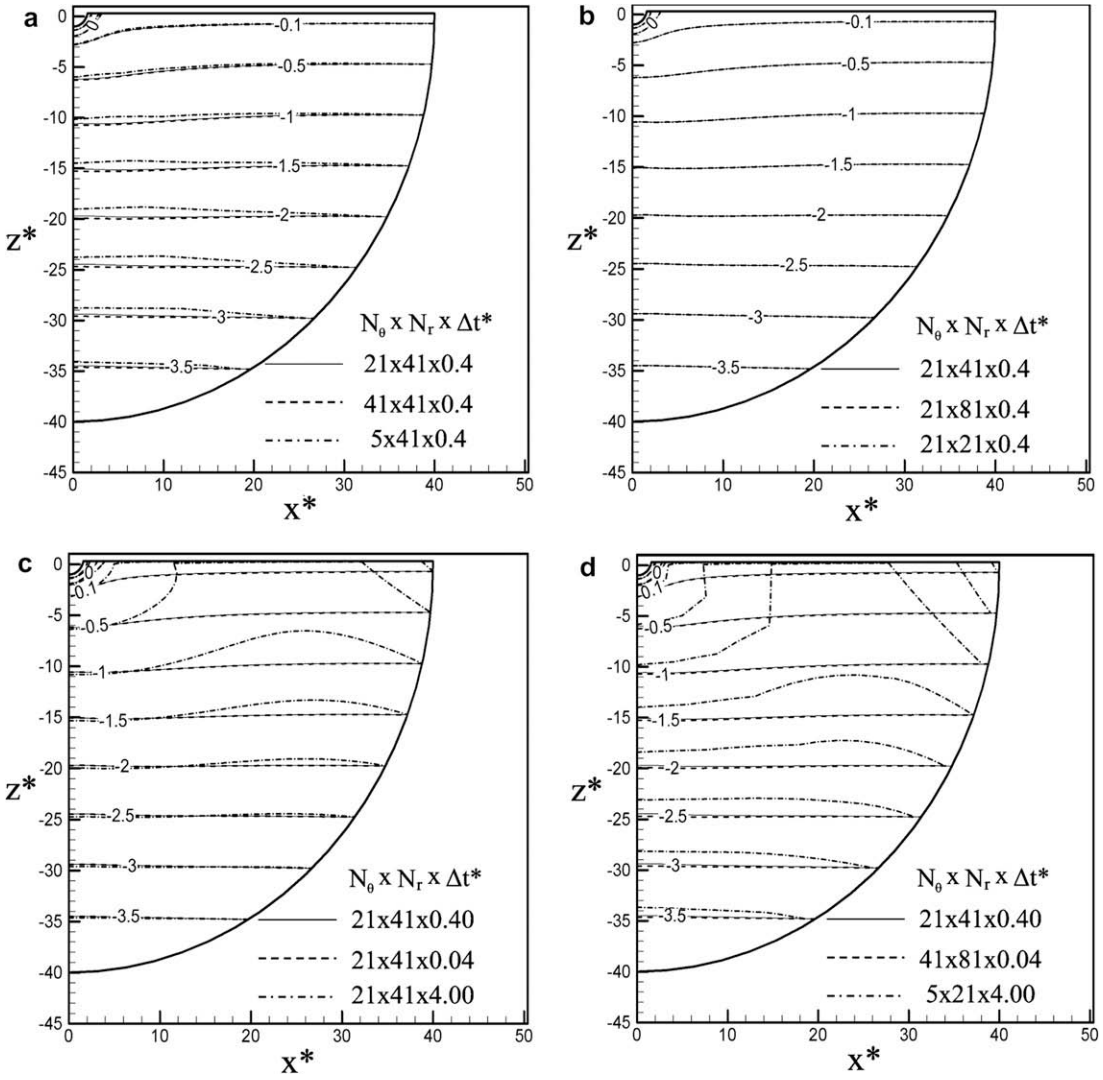

Fig. 3. Convergence test by varying grids in (a) longitudinal direction, (b) radial direction, (c) time, and (d) longitudinal, radial and time.

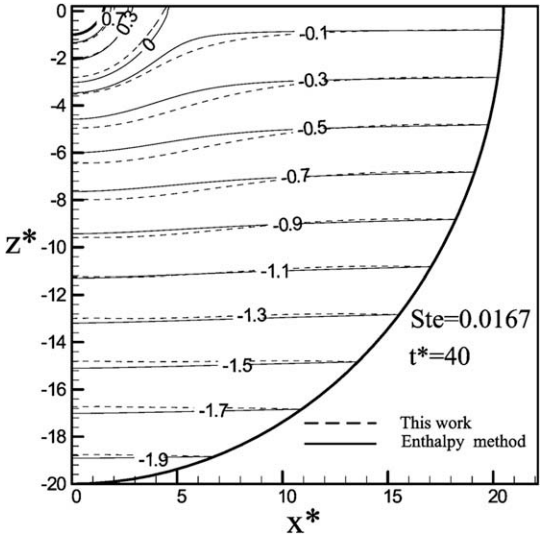

Fig. 4. Comparisons of predicted dimensionless temperature fields and fusion zone shapes between finite-difference method [45] and this work.

the solid and dashed lines, respectively, represent the isothermal lines obtained from the finite-difference solution of the enthalpy equation and this work. Dimensionless temperature of unity refers to the inner surface, while the isothermal line of zero temperature indicates the outer boundary of the molten layer. In view of heat transfer from the higher temperature at the bubble surface, the solid is melted as a thin layer around the inner surface. Heat can also be transferred from higher temperature of the liquid above the solidification front into the solid. Thus heat transfer far away from the bubble is unidirectional, while that near the bubble is radial. Uniform spacing between isothermal lines reflects constant temperature gradient in the solid region far from the bubble. Dense spacing between the isothermal lines implies high heat flux near the bubble. To compare the finite-difference solution, initial coefficients of temperatures in liquid and solid are chosen to be $b = -0.12$, and $b' = -10^{-6}$, respectively, while the initial contour of the liquid layer is

$$r^*_{m0} = 25.2650 - 30.7184\theta + 16.7135\theta^2 - 4.2190\theta^3 + 0.4091\theta^4 \quad (34)$$

The initial temperature field of this work thus agrees well with that of the finite-difference method. This figure finds that the solution provided in this work agrees with the finite-difference solution. Even though the initial temperature was arbitrarily chosen, the deviation between two methods decreased with increasing time. The relevancy of this work is thus confirmed.

Two constraints are required to determine two coefficients of the assumed quadratic temperature distribution in each phase, as discussed previously. In view of the irregular shapes of distinct phases, temperature coefficients are determined in three ways in this work. That is, temperature coefficients in the liquid layer between $\theta_{ie} \leqslant \theta \leqslant \theta_{me}$ are determined by given two boundary conditions Eqs. (26) and (27). Two coefficients in the liquid layer for angles $\theta_{me} \leqslant \theta \leqslant \pi$ are determined by solving Eqs. (19) and (26) subject to the axisymmetric boundary condition, and boundary condition equation (27) at the edge angle θ_{me}. In the solid region, Eq. (28) and the fictitious boundary condition equation (29) are introduced to determine temperature coefficients with angles between $\theta_{me} \leqslant \theta \leqslant \theta_{Re}$. This is consistent with the fact that the temperature profile (or velocity profile in boundary layer) must be chosen as a prior condition in the integral approximation method. Determinations of temperature coefficients for the angle between $\theta_{Re} \leqslant \theta \leqslant \pi$ require solving Eq. (20) subject to the axisymmetric condition, boundary condition equations (30) and (28) at θ_{Re}.

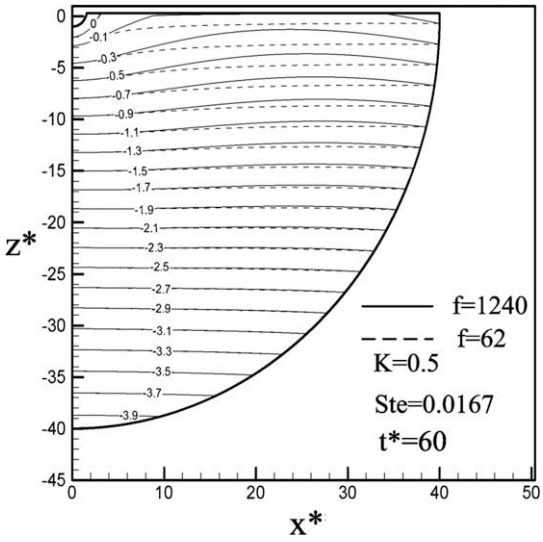

Fig. 5. Effect of dimensionless fictitious distance on temperature fields.

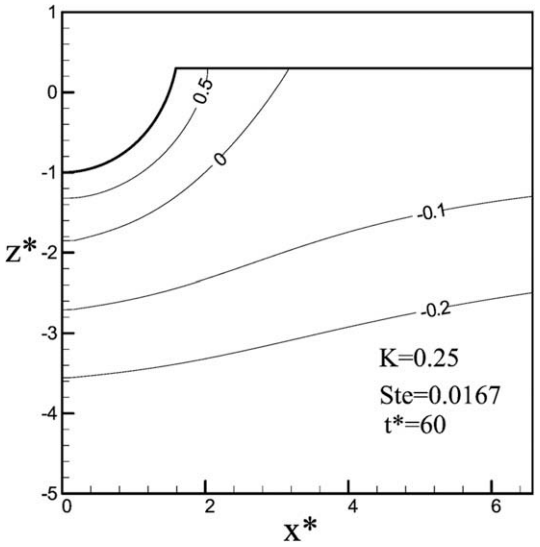

Fig. 7. Dimensionless temperature fields and fusion zone shape in liquid and solid at $t^* = 60$ for thermal conductivity ratio $K = 0.25$.

The effects of the fictitious boundary condition on temperature fields around the bubble or particle are seen in Fig. 5. A significant increase by 20 times in the dimensionless fictitious distance results in non-flat isothermal lines near the middle region and solidification front. Interestingly, the effects of the fictitious distance on thermal fields are insignificant. This agrees with the well-known fact that the effects of temperature (or velocity) profile on energy (or momentum) transport in the integral approximation methods are insignificant. Computations also showed that deviation is reduced, provided that the outer radius of the system R^* is chosen to be larger.

Fig. 6(a) and (b) shows the predicted dimensionless temperature fields in liquid and solid at dimensionless time $t^* = 8$ and 60, respectively. Dimensionless times correspond to 2 and 15 s, respectively, for the freezing of water and melting of ice. It can be seen that the solidification front proceeds and the region of the molten layer expands as time increases. This is attributed to the fact that heat transfer from the liquid and bubble to the solid is greater than that dissipated to the surroundings by cooling at

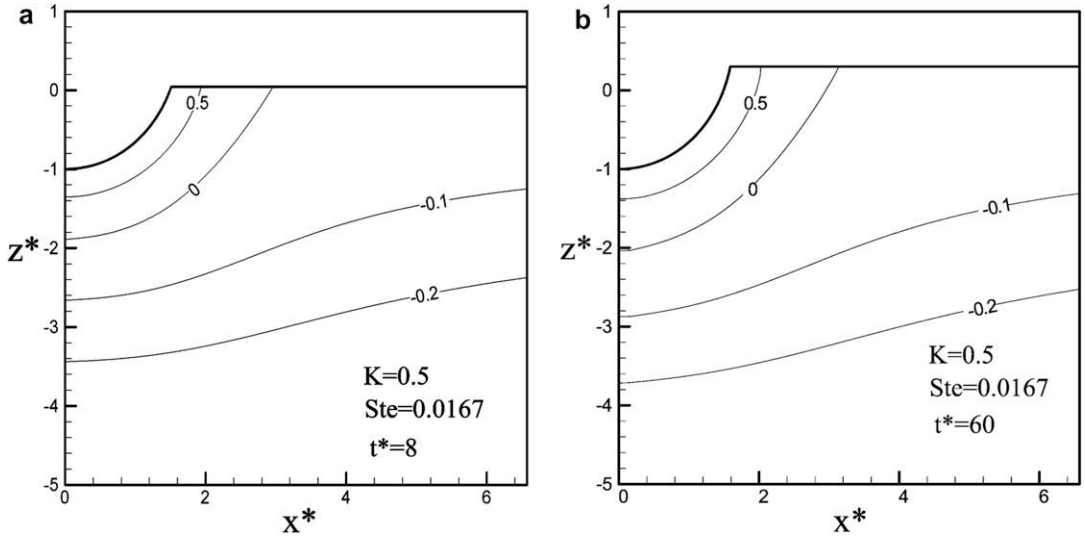

Fig. 6. Dimensionless temperature fields in liquid and solid predicted from this work at dimensionless time (a) $t^* = 8$, and (b) $t^* = 60$.

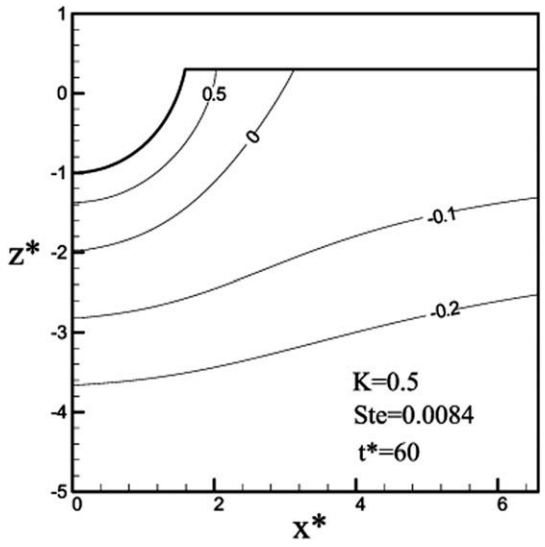

Fig. 8. Dimensionless temperature fields and fusion zone shape in liquid and solid at $t^* = 60$ for Stefan number $Ste = 0.0084$.

an early stage. Computations also showed that thickness of the molten layer may be either decreased or increased in the course of freezing. The results will be presented in a future work.

Fig. 7 shows the effects of the liquid-to-solid thermal conductivity ratio on dimensionless temperature fields in a liquid and a solid. Referring to Fig. 6(b), a decrease in the liquid-to-solid thermal conductivity ratio or an increase in solid thermal conductivity reduces the thickness of the liquid layer. The reason for this is that latent heat for melting decreases due to an increase in heat conduction into solid, as can be seen from the Stefan boundary condition. In view of the increase in latent heat seen in Fig. 6(b), a decrease in Stefan number reduces the thickness of the liquid layer, as shown in Fig. 8.

4. Conclusions

The following conclusions can be drawn:

1. Temperature distributions in the molten layer and solid with distinct properties around a bubble or particle entrapped in solid during unidirectional solidification are determined by applying the heat-balance integral method. The heat-balance equations are derived by integrating unsteady elliptic heat conduction equations and introducing the Stefan boundary condition. Since the number of independent variables is reduced by one, the heat-balance integral method is a good tool to study moving boundary problems experiencing phase changes. Computed results agree with finite-difference solutions of enthalpy equations and physical interpretation.
2. Due to the time-dependent irregular shapes of phases, the coefficients of assumed quadratic temperature profiles are considered to be functions of longitudinal coordinate and time. Two temperature coefficients in each phase can be determined by (a) one boundary condition and the equation governing temperature coefficient obtained from the heat-balance integral equation, (b) two boundary conditions, and (c) one boundary condition and an introduced fictitious boundary condition. The fictitious boundary condition used to determine coefficients encountered in an irregular physical domain leads to good results.
3. It would be worthwhile extending this method to solve unsteady convective elliptic problems with phase changes in irregular shapes. Furthermore, the time-dependent surface of the bubble or inner surface of the system can also be straightforwardly extended with challenging. However, this requires an inclusion of the Rayleigh–Plesset or the Young–Laplace equation for a complicated analysis.

Appendix A

Initial temperature coefficients a_{l0}, b_{l0}, a_{s0}, b_{s0} are determined as follows:

Initial liquid temperature is given by

$$T_{l0} = (T_i - T_m)\left[a(r^* - r_i^*)^2 + b(r^* - r_i^*) + c\right] \tag{A1}$$

where a, b and c are constants. The degree of Eq. (A1) can be selected to be higher than quadratic to obtain more accurate results. Coefficients in Eq. (A1) are determined by satisfying boundary conditions

$$T_{l0} = T_i \text{ at } r^* = r_i^*, \quad \text{and} \quad T_{l0} = T_m \text{ at } r^* = r_{m0}^* \tag{A2}$$

Dimensionless initial temperature in the liquid layer then yields

$$\psi_{l0} = 1 - \left(b + \frac{1}{r_{m0}^* - r_i^*}\right)\frac{(r^* - r_i^*)^2}{(r_{m0}^* - r_i^*)} + b(r^* - r_i^*) \tag{A3}$$

Energy function of liquid in Eq. (14) by substituting Eq. (A3) gives

$$\begin{aligned} H_{l0}^* = {} & \frac{1}{3}(r_{m0}^{*3} - r_i^{*3}) - \left(b + \frac{1}{r_{m0}^* - r_i^*}\right)(r_{m0}^* - r_i^*)^{-1} \\ & \times \left[\frac{1}{5}(r_{m0}^{*5} - r_i^{*5}) - \frac{1}{2}r_i^*(r_{m0}^{*4} - r_i^{*4}) + \frac{r_i^{*2}}{3}(r_{m0}^{*3} - r_i^{*3})\right] \\ & + b\left[\frac{1}{4}(r_{m0}^{*4} - r_i^{*4}) - \frac{r_i^*}{3}(r_{m0}^{*3} - r_i^{*3})\right] \end{aligned} \tag{A4}$$

Comparing Eq. (A4) with Eq. (23) subject to Eq. (26), respectively, gives

$$\begin{aligned} b_{l0} = {} & \left\{\frac{1}{\delta_0^*}\left(\frac{r_{m0}^* r_i^{*3}}{3} - \frac{r_i^{*4}}{4} - \frac{r_{m0}^{*4}}{12}\right) + \frac{1}{3}(r_{m0}^{*3} - r_i^{*3}) - \frac{1}{\delta_0^*}\left(b + \frac{1}{\delta_0^*}\right)\right. \\ & \times \left[\frac{1}{5}(r_{m0}^{*5} - r_i^{*5}) - \frac{r_i^*}{2}(r_{m0}^{*4} - r_i^{*4}) + \frac{r_i^{*2}}{3}(r_{m0}^{*3} - r_i^{*3})\right] \\ & \left. + b\left[\frac{1}{4}(r_{m0}^{*4} - r_i^{*4}) - \frac{r_i^*}{3}(r_{m0}^{*3} - r_i^{*3})\right]\right\}\left[\delta_0^*\left(\frac{r_{m0}^* r_i^{*3}}{3} - \frac{r_i^{*4}}{4} - \frac{r_{m0}^{*4}}{12}\right)\right. \\ & \left. + \frac{r_{m0}^{*5}}{30} - \frac{r_{m0}^{*2} r_i^{*3}}{3} + \frac{r_i^{*4} r_{m0}^*}{2} - \frac{r_i^{*5}}{5}\right]^{-1} \end{aligned} \tag{A5}$$

$$a_{l0} = \delta_0^* b_{l0} - \frac{1}{\delta_0^*} \tag{A6}$$

Similarly, temperature distribution in the solid is considered to be

$$T_{s0} = (T_i - T_m)\left[a'(r^* - r_{m0}^*)^2 + b'(r^* - r_{m0}^*) + c'\right] \tag{A7}$$

subject to boundary conditions

$$T_{s0} = T_m \text{ at } r^* = r_{m0}^*, \quad \text{and} \quad T_{s0} = T_m + zg_0 \text{ at } r^* = R^* \tag{A8}$$

Distributions of dimensionless temperature and energy in the solid, respectively, lead to

$$\psi_{s0} = \left[R^* g_0^* \cos\theta_0 - b'\left(R^* - r_{m0}^*\right)\right]\left(\frac{r^* - r_{m0}^*}{R^* - r_{m0}^*}\right)^2 + b'\left(r^* - r_{m0}^*\right) \quad \text{(A9)}$$

$$\begin{aligned} H_{s0}^* = {} & \left[R^* g_0^* \cos\theta_0 - b'\left(R^* - r_{m0}^*\right)\right]\left(R^* - r_{m0}^*\right)^{-2} \\ & \times \left[\frac{1}{5}\left(R^{*5} - r_{m0}^{*5}\right) - \frac{1}{2} r_{m0}^*\left(R^{*4} - r_{m0}^{*4}\right) + \frac{r_{m0}^{*2}}{3}\left(R^{*3} - r_{m0}^{*3}\right)\right] \\ & + b'\left[\frac{1}{4}\left(R^{*4} - r_{m0}^{*4}\right) - \frac{r_{m0}^*}{3}\left(R^{*3} - r_{m0}^{*3}\right)\right] \end{aligned} \quad \text{(A10)}$$

Eq. (A10) by comparing to Eq. (24) gives

$$\begin{aligned} b_{s0} = {} & \left\{ -\frac{g_0^*}{\delta_{R0}^*} R^* \cos\theta_0 \left(\frac{R^{*4}}{4} - \frac{r_{m0}^* R^{*3}}{3} + \frac{r_{m0}^{*4}}{12}\right) + \delta_{R0}^{*-2}\left(R^* g_0^* \cos\theta_0 - b'\delta_{R0}^*\right) \right. \\ & \times \left[\frac{1}{5}\left(R^{*5} - r_{m0}^{*5}\right) - \frac{1}{2} r_{m0}^*\left(R^{*4} - r_{m0}^{*4}\right) + \frac{r_{m0}^{*2}}{3}\left(R^{*3} - r_{m0}^{*3}\right)\right] \\ & \left. + b'\left[\frac{1}{4}\left(R^{*4} - r_{m0}^{*4}\right) - \frac{r_{m0}^*}{3}\left(R^{*3} - r_{m0}^{*3}\right)\right]\right\} \\ & \times \left[\frac{R^{*5}}{5} - \frac{R^{*4} r_{m0}}{2} + \frac{R^{*3} r_{m0}^{*2}}{3} - \frac{r_{m0}^{*5}}{30} - \delta_{R0}^*\left(\frac{R^{*4}}{4} - \frac{r_{m0}^* R^{*3}}{3} + \frac{r_{m0}^{*4}}{12}\right)\right]^{-1} \end{aligned} \quad \text{(A11)}$$

where Eq. (28) at the initial time

$$a_{s0} = \frac{g_0^*}{\delta_{R0}^*} R^* \cos\theta_0 - b_{s0}\delta_{R0}^* \quad \text{(A12)}$$

is introduced. Initial temperature coefficients as a function of longitudinal coordinate in the liquid layer and solid region therefore are calculated from Eqs. (A5), (A6), (A11) and (A12), respectively, by specifying constant coefficients b and b'.

References

[1] H.C. Carslaw, J.C. Jaeger, Conduction of Heat in Solids, Clarendon Press, Oxford, 1959.
[2] J. Crank, Free and Moving Boundary Problems, Clarendon Press, Oxford, 1984.
[3] T.R. Goodman, Application of integral methods to transient nonlinear heat transfer, in: T.F. Irvine, J.P. Hartnett (Eds.), Advances in Heat Transfer, Academic Press, New York, 1964, pp. 51–122.
[4] H. Schlichting, Boundary-Layer Theory, seventh ed., McGraw-Hill, New York, 1979.
[5] T.R. Goodman, The heat-balance integral and its application to problems involving a change of phase, Trans. ASME 80 (1958) 335–342.
[6] T.R. Goodman, J.J. Shea, The melting of finite slabs, J. Appl. Mech. 27 (1960) 16–24.
[7] G. Poots, An approximate treatment of a heat conduction problem involving a two-dimensional solidification front, Int. J. Heat Mass Transfer 5 (1962) 339–348.
[8] D.S. Riley, P.W. Duck, Application of the heat-balance integral method to the freezing of a cuboid, Int. J. Heat Mass Transfer 20 (1977) 294–296.
[9] H. Rasmussen, An approximate method for solving two-dimensional Stefan problems, Lett. Heat Mass Transfer 4 (1977) 273–277.
[10] A. Kharab, An approximate method for the solution of a three-dimensional free boundary problem arising in hydraulics, Comput. Meth. Appl. Mech. Eng. 148 (1997) 187–194.
[11] P.S. Wei, C.C. Huang, K.W. Lee, Nucleation of bubbles on a solidification front-experiment and analysis, Metall. Mater. Trans. B 34B (2003) 321–332.
[12] J.C. Tannehill, D.A. Anderson, R.H. Pletcher, Computational Fluid Mechanics and Heat Transfer, Taylor & Francis, New York, 1997.
[13] J.F. Thompson, Z.U.A. Warsi, C.W. Mastin, Numerical Grid Generation: Foundations and Applications, North-Holland, Amsterdam, 1985.
[14] W.R. Wilcox, V.H.S. Kuo, Gas bubble nucleation during crystallization, J. Cryst. Growth 19 (1973) 221–228.
[15] S.F. Jones, G.M. Evans, K.P. Galvin, Bubble nucleation from gas cavities – a review, Adv. Colloid Interf. Sci. 80 (1999) 27–50.
[16] K.F. Vasconcellos, J. Beech, The development of blowholes in the ice/water/carbon dioxide system, J. Cryst. Growth 28 (1975) 85–92.
[17] K. Tagavi, L.C. Chow, O. Solaiappan, Void formation in unidirectional solidification, Exp. Heat Transfer 3 (1990) 239–255.
[18] K. Murakami, H. Nakajima, Formation of pores during unidirectional solidification of water containing carbon dioxide, Mater. Trans. 43 (2002) 2582–2588.
[19] K.A. Mørch, Cavitation nuclei and bubble formation – a dynamic liquid–solid interface problem, J. Fluids Eng. 122 (2000) 494–498.
[20] H. Jamgotchian, R. Trivedi, B. Billia, Interface dynamics and coupled growth in directional solidification in presence of bubbles, J. Cryst. Growth 134 (1993) 181–195.
[21] M.V.A. Bianchi, R. Viskanta, The effect of air bubbles on the diffusion-controlled solidification of water and aqueous solutions of ammonium chloride, Int. J. Heat Mass Transfer 42 (1999) 1097–1110.
[22] T. Tao, X.F. Peng, D.J. Lee, Force of a gas bubble on a foreign particle in front of a freezing interface, J. Colloid Interf. Sci. 280 (2004) 409–416.
[23] P.S. Wei, C.Y. Ho, An analytical self-consistent determination of a bubble with a deformed cap trapped in solid during solidification, Metall. Mater. Trans. B 33B (2002) 91–100.
[24] P.S. Wei, C.C. Huang, Z.P. Wang, K.Y. Chen, C.H. Lin, Growths of bubble/pore sizes in solid during solidification – an in situ measurement and analysis, J. Cryst. Growth 270 (2004) 662–673.
[25] G.F. Bolling, J. Cisse, A theory for the interaction of particles with a solidifying front, J. Cryst. Growth 10 (1971) 56–66.
[26] P. Casses, M.A. Azouni, Thermal effects on the shape of a solidifying interface near a foreign particle, J. Cryst. Growth 130 (1993) 13–20.
[27] A.A. Chernov, D.E. Temkin, A.M. Mel'nikova, Theory of the capture of solid inclusions during the growth of crystals from the melt, Sov. Phys. Crystallogr. 21 (1976) 369–374.
[28] S.S. Babu, S.A. David, J.M. Vitek, K. Mundra, T. DebRoy, Development of macro- and microstructures of carbon–manganese low alloy steel welds-inclusion formation, Mater. Sci. Technol. 11 (1995) 186–199.
[29] Ch. Körber, G. Rau, M.D. Cosman, E.G. Cravalho, Interaction of particles and a moving ice–liquid interface, J. Cryst. Growth 72 (1985) 649–662.
[30] M.K. Moallemi, R. Viskanta, Analysis of close-contact melting heat transfer, Int. J. Heat Mass Transfer 29 (1986) 855–867.
[31] M.K. Moallemi, R. Viskanta, B.W. Webb, An experimental and analytical study of close-contact melting, ASME J. Heat Transfer 108 (1986) 894–899.
[32] A. Bejan, Convection Heat Transfer, Wiley, New York, 1995.
[33] S.A. Fomin, P.S. Wei, V.A. Chugunov, Contact melting by a non-isothermal heating surface of arbitrary shape, Int. J. Heat Mass Transfer 38 (1995) 3275–3284.
[34] J.J. Batteh, M.M. Chen, J. Mazumder, A stagnation flow-analysis of the heat transfer and fluid-flow phenomena in laser drilling, J. Heat Transfer 122 (2000) 801–807.
[35] P.S. Wei, L.R. Chiou, Molten metal flow around the base of a cavity during a high-energy beam penetrating process, ASME J. Heat Transfer 110 (1988) 918–923.
[36] P.S. Wei, J.Y. Ho, Energy considerations in high-energy beam drilling, Int. J. Heat Mass Transfer 33 (1990) 2207–2217.
[37] V.S. Arpaci, Conduction Heat Transfer, Addison-Wesley, New York, 1966.
[38] M.N. Özisik, Heat Conduction, Wiley, New York, 1980.
[39] S.B.G. O'Brien, On the shape of small sessile and pendant drops by singular perturbation techniques, J. Fluid Mech. 233 (1991) 519–537.
[40] R. Viskanta, Heat transfer during melting and solidification of metals, 50th anniversary issue, ASME J. Heat Transfer 110 (1988) 1205–1219.
[41] D. Frederick, R. Greif, A method for the solution of heat transfer problems with a change of phase, J. Heat Transfer 107 (1985) 520–526.
[42] B.J. Noye, Part 1: Numerical methods, an introduction to finite-difference techniques, in numerical simulation of fluid motion, in: J. Noye (Ed.), Proceedings of an International Conference on the Numerical Simulation of Fluid Dynamic Systems, Monash University, Melbourne, 1976, North-Holland, Amsterdam, 1978, pp. 1–112.
[43] S.V. Patankar, Numerical Heat Transfer and Fluid Flow, Hemisphere, New York, 1980.
[44] M.S. Plesset, A. Prosperetti, Bubble dynamics and cavitation, Annu. Rev. Fluid Mech. 9 (1977) 145–185.
[45] K.R. Lin, M.S. Thesis, Mechanical and Electro-Mechanical Engineering, National Sun Yat-Sen University, 2005.